

γ -Ray-Triggered Drug Release of Reactive Oxygen Species-Sensitive Nanomedicine for Enhanced Concurrent Chemoradiation Therapy

Ying Yu, Zujian Feng, Jinjian Liu, Xiaoxue Hou, Xiaoqian Zhou, Jie Gao, Wei Wang, Yumin Zhang,* Guoliang Li,* and Jianfeng Liu*



Cite This: *ACS Omega* 2021, 6, 19445–19457



Read Online

ACCESS |



Metrics & More

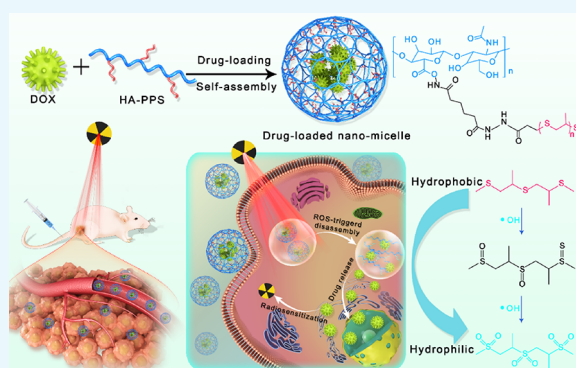


Article Recommendations



Supporting Information

ABSTRACT: Radiotherapy (RT) combined with chemotherapy remains a dominant therapeutic manner in clinical tumor treatment, which is irreplaceable in a short term. To seek an intrinsic connection of combined chemoradiation therapy and maximize the antitumor efficacy, we developed a reactive oxygen species (ROS)-sensitive nanomicelle drug delivery system based on a self-assembled amphiphilic polymer, hyaluronic acid-*graft*-poly-(propylene sulfide) (HA-PPS). A chemical radiosensitizer, doxorubicin (DOX), was encapsulated into the core of HA-PPS nanomicelles, constituting the DOX-loaded nanomicelles (HA-PPS@DOX NMs) with a spherical structure of around 205.10 ± 11.33 nm diameter with a narrow polydispersity index (PDI) of 0.135 ± 0.01 . When combined with RT, the ROS-sensitive HA-PPS@DOX NMs disintegrated and released great drug cargos, which further enhanced cytotoxicity. Meanwhile, as a radiosensitizer, the released DOX sensitized cancer cells to radiotherapy, which has been confirmed by an enhanced sensitizer enhancement ratio (SER) value of 1.78 contributing to the increased cytotoxicity of concurrent chemoradiation tumor therapy, as evidenced by the improvement of half maximal inhibitory concentration (IC_{50} value) of DOX from 2.316 to 0.8235 $\mu\text{g}/\text{mL}$. Moreover, *in vivo* studies revealed that HA-PPS@DOX NMs exhibited prolonged circulation time and improved tumor accumulation. Particularly, the released DOX triggered by radiation strengthened radiotherapy sensitization in return. Consequently, these superiorities of HA-PPS@DOX NMs shown by the concurrent chemoradiation tumor therapy resulted in an ideal tumor inhibition rate of 70.4%, thus providing a promising ROS-sensitive nanomedicine for cancer treatment.



INTRODUCTION

Varieties of cancer therapy strategies have been widely studied and applied in clinical treatments, including chemotherapy,^{1,2} radiotherapy,^{3–6} immunotherapy,^{7–10} gene therapy,^{11,12} photodynamic therapy,^{13–16} and photothermal therapy.^{17–20} However, it is often difficult to get the expected effect for the limited curative efficacy and drug resistance after repeated treatments using a single therapy. To optimize the antitumor performance, combination treatments based on the above tumor therapies emerged and acquired satisfactory clinical outcomes.^{21–25} Cocktail treatment, a classic combination strategy, which has been widely used for different kinds of diseases, increased the survival rate of people with advanced melanoma during the clinical treatment.²⁶ A sequential combination strategy, another common clinical therapy, has become a standard of care for breast cancer and other cancer types, providing early access for improving the survival rate.²⁷ Both of these clinical results exhibited a promising antitumor efficiency of combination therapies, which indeed prolonged overall survival and progression-free survival. To date, the combination of chemotherapy and radiation therapy has been

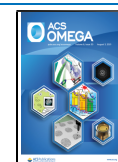
set as a standard in many solid tumor treatments,³ including concurrent chemoradiation therapy, sequential chemoradiation therapy, and alternate chemoradiation therapy. However, despite the improved therapeutic outcomes shown by combined chemoradiation therapy, more intelligent platforms or carriers are still urgently needed to be developed to coordinate and optimize the parameters of combination treatments to maximize their antitumor efficiency as well as reduce the severe side effects.

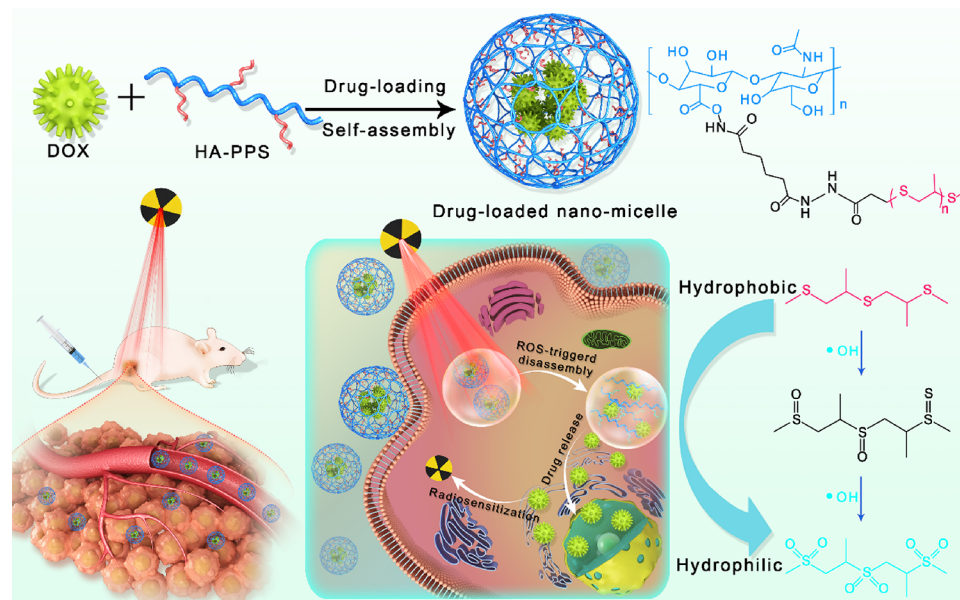
Nanomaterials have been widely used for constructing drug delivery systems due to their unique features of an enhanced permeability and retention (EPR) effect and stimulus-responsive drug release.^{28–31} Hence, smart nanoparticles were a kind of ideal carrier for concurrently combining

Received: March 20, 2021

Accepted: July 7, 2021

Published: July 22, 2021



Scheme 1. Illustration of the Concurrent Chemoradiation Therapy Based on the HA-PPS@DOX NMs^a

^aHA-PPS@DOX NMs arrived at tumor sites and largely accumulated after *i.v.* injection. Upon radiation, PPS was oxidized to hydrophilic sulfoxides/sulfone, leading to the disassembly of HA-PPS nanomicelles. The released DOX acted on nuclei as well as sensitized cells to radiation, enhancing efficacy of concurrent chemoradiation therapy.

chemotherapy and radiotherapy. As reported by Liu *et al.*,³² they constructed radionuclide ¹³¹I-labeled albumin-paclitaxel nanoparticles, realizing integration of chemotherapy and radioisotope therapy *in vivo* with high synergistic efficacy. In another work by Dong *et al.*,³³ a thermosensitive micellar hydrogel simultaneously loaded with the ¹³¹I radioisotope and doxorubicin was applied for tumor chemoradiation treatment. Nevertheless, among these strategies, radiation and chemotherapy were just simply combined rather than their advantages being maximized. Actually, some chemotherapeutic agents like paclitaxel³⁴ and cisplatin³⁵ are also known as radiosensitizers in clinical concurrent chemoradiation therapy and indeed establish a bridge for connection of these two therapeutic manners. However, such combined strategies brought aggravated side effects that were unbearable for patients. Recently, some unique nanocarriers that can respond to the tumor microenvironment (acidic pH, hypoxia, high-level reactive oxygen species (ROS)/glutathione (GSH)) have attracted great attention for their merits of responsive drug release within tumor sites, enhanced specificity to tumor tissues, and alleviated side effects on healthy tissues.^{36–38} It has been reported that there is a large amount of ROS in tumor sites, and extra ROS could also be produced by radiotherapy. Therefore, we hypothesized that the amount of ROS produced by the external beam radiation therapy (EBRT) can be used as a switch to trigger the disassembly of ROS-sensitive nanocarriers for controlled drug release, which can realize a specific chemotherapy during the process of RT via *in situ* radiation-induced drug release within tumor sites.

Here, we developed an ROS-sensitive nanoplatform loaded with the chemical radiosensitizer doxorubicin (DOX) to constitute a multifunctional intelligent nanomedicine (denoted as HA-PPS@DOX) for highly efficient concurrent chemoradiation tumor therapy. As illustrated in Scheme 1, nanomicelles (HA-PPS) were prepared using the self-assembly amphiphilic polymer, where poly(propylene sulfide) (PPS) is

the hydrophobic segment and hyaluronic acid (HA) is the hydrophilic segment. The clinical broad-spectrum chemotherapeutic agent, DOX, which can damage DNA by inhibiting topoisomerase II⁴⁰ and sensitize cells to radiation,⁴¹ was loaded into the inner core of ROS-responsive nanocarriers by hydrophobic interaction. It has been reported that the hydrophobic PPS will be oxidized into hydrophilic sulfoxides/sulfone once suffering from RT,³⁹ thus leading to the disassembly of HA-PPS nanomicelles. HA-PPS@DOX NMs arrived at tumor sites through systematic circulation and accumulated at the tumor site due to the EPR effect after being intravenously injected *in vivo*. At this juncture, local radiotherapy intervenes and triggers the DOX release at the tumor site, achieving a specific tumor chemotherapy; meanwhile, the released DOX as a radiosensitizer would further enhance the cell sensitivity to radiotherapy, thus tremendously promoting the antitumor effect of concurrent chemoradiation therapy.

RESULTS AND DISCUSSION

Preparation of Polymers and Drug-Loaded Nanomicelles (NMs). The hydrophobic PPS segment was synthesized through ring-opening polymerization according to Figure S1, and its successful synthesis was confirmed by ¹H NMR (Figure S2). Then, PPS was coupled to HA through a series of amidation reactions (Figure S1), which was confirmed by the ¹H NMR spectrum (Figure 1a), the peak at 1.95 ppm was attributed to protons of N-acetyl groups in HA molecules, and characteristic peaks at 1.37–1.38, 2.62, and 2.90–2.92 ppm belonged to PPS. As shown in the FTIR spectrum (Figure 1b), the absorption bands at 3433.67, 2955.67–2850.04, and 1573.57 cm⁻¹ could be attributed to the vibration of O–H, C–H, and N–H bonds, respectively, further confirming the successful synthesis of the HA-PPS polymer.

Subsequently, spherical nanomicelles of HA-PPS with a diameter of about 174.42 ± 9.67 nm (Figure 1c) were prepared through an oil-in-water (o/w) method. Then, the

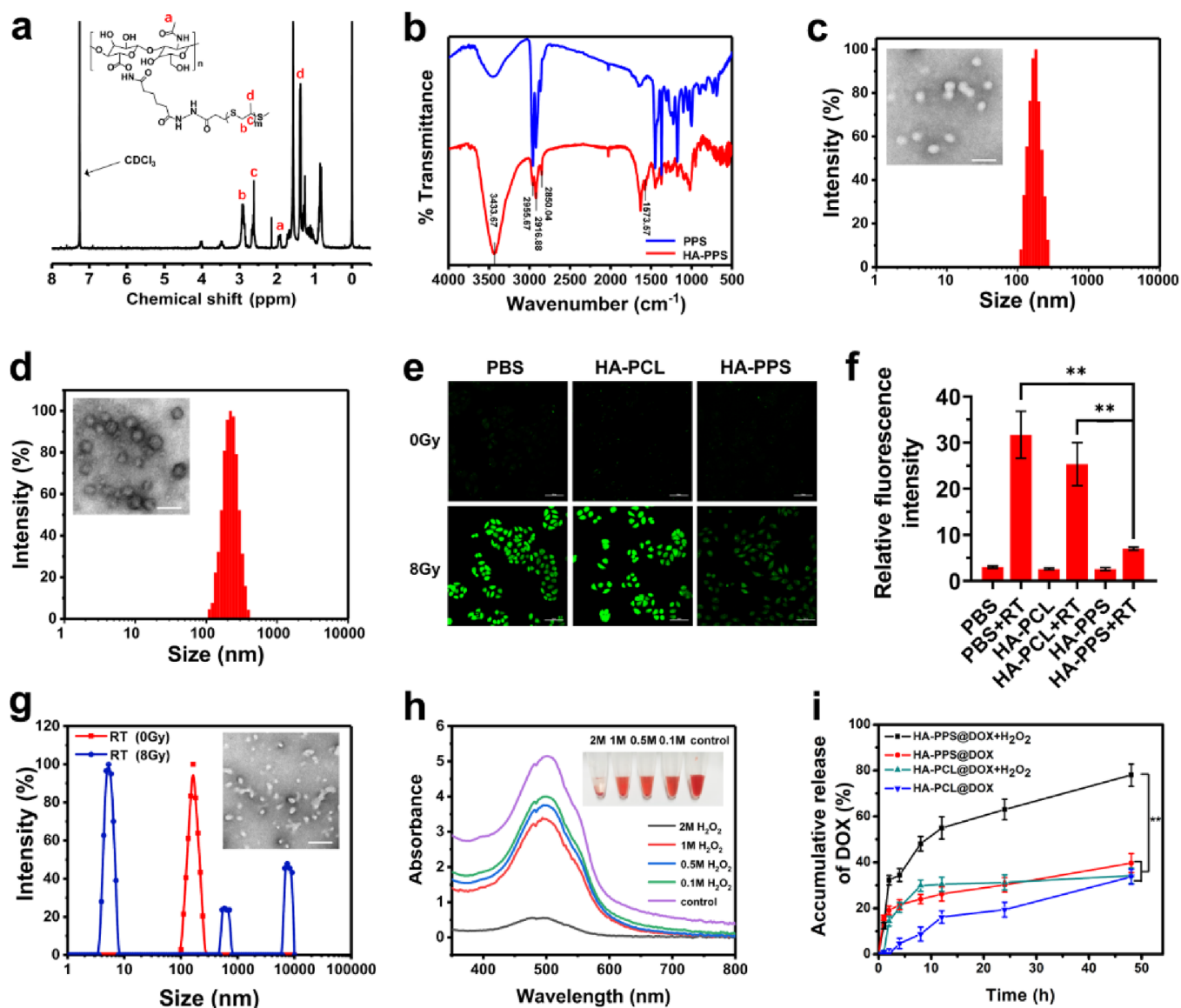


Figure 1. Characterization of ROS-responsive HA-PPS@DOX NMs. (a) ^1H NMR spectrum of the HA-PPS polymer (dissolved in CDCl_3). (b) FTIR spectra of PPS and HA-PPS polymers. Diameter and TEM images of HA-PPS NMs (c) and HA-PPS@DOX NMs (d). Scale bar: 500 nm. CLSM images (e) and quantitative analysis (f) of the ROS level within MCF-7 cells after treatment with PBS, HA-PCL NMs (100 $\mu\text{g}/\text{mL}$), and HA-PPS NMs (100 $\mu\text{g}/\text{mL}$) with or without γ -ray radiation. Scale bar: 50 μm . Data were presented as mean \pm SD ($n = 3$), $**p < 0.01$. (g) Disassembly of HA-PPS NMs after 8 Gy radiation by DLS and TEM characterization. Scale bar: 500 nm. (h) UV-vis spectrum of HA-PPS@DOX after incubation with various concentrations of hydrogen peroxide (H_2O_2). (i) H_2O_2 -triggered release of DOX from HA-PPS NMs and HA-PCL NMs. Data were presented as mean \pm SD ($n = 3$), $**p < 0.01$.

DOX-loaded nanomicelles (HA-PPS@DOX NMs) were prepared by hydrophobic interaction between free DOX and HA-PPS NMs. TEM images showed that HA-PPS@DOX NMs exhibited a spherical morphology and were uniform in size with a narrow polydispersity index (PDI) of 0.135 ± 0.01 , which was approximately 205.10 ± 11.33 nm as determined by DLS results (Figure 1d). The zeta potential of HA-PPS@DOX NMs was -22.32 ± 2.19 mV, showing no obvious difference with HA-PPS micelles (-25.4 ± 3.62 mV). In addition, by comparing the ultraviolet (UV-vis) absorption spectrum, we found that neither the peak shape nor the maximum absorption peak of DOX changed after being loaded into HA-PPS NMs (Figure S3), suggesting that DOX had been successfully encapsulated. In addition, the drug loading content (DLC) and drug loading efficiency (DLE) of HA-PPS@DOX

NMs were 18.13 and 87.02%, respectively, showing a high drug loading capacity of HA-PPS NMs.

ROS-Responsive Drug Release of Nanomicelles. First, in order to confirm the ROS-responsive capacity of HA-PPS, a DCFH-DA probe was adopted to test the intracellular ROS level. As depicted in Figure 1e, compared with nonradiation (0 Gy) groups, cells incubated with PBS or HA-PCL (a control group that has no response to ROS whose structural information is shown in Figure S4) exhibited strong fluorescence intensity after γ -ray radiation (8 Gy), indicating that a large amount of ROS was produced in cells after radiation. However, only very weak ROS signals were observed in HA-PPS groups (Figure 1f), which can be attributed to the consumption of ROS by PPS. In other words, PPS has been oxidized by the reduced ROS and may thus lead to the

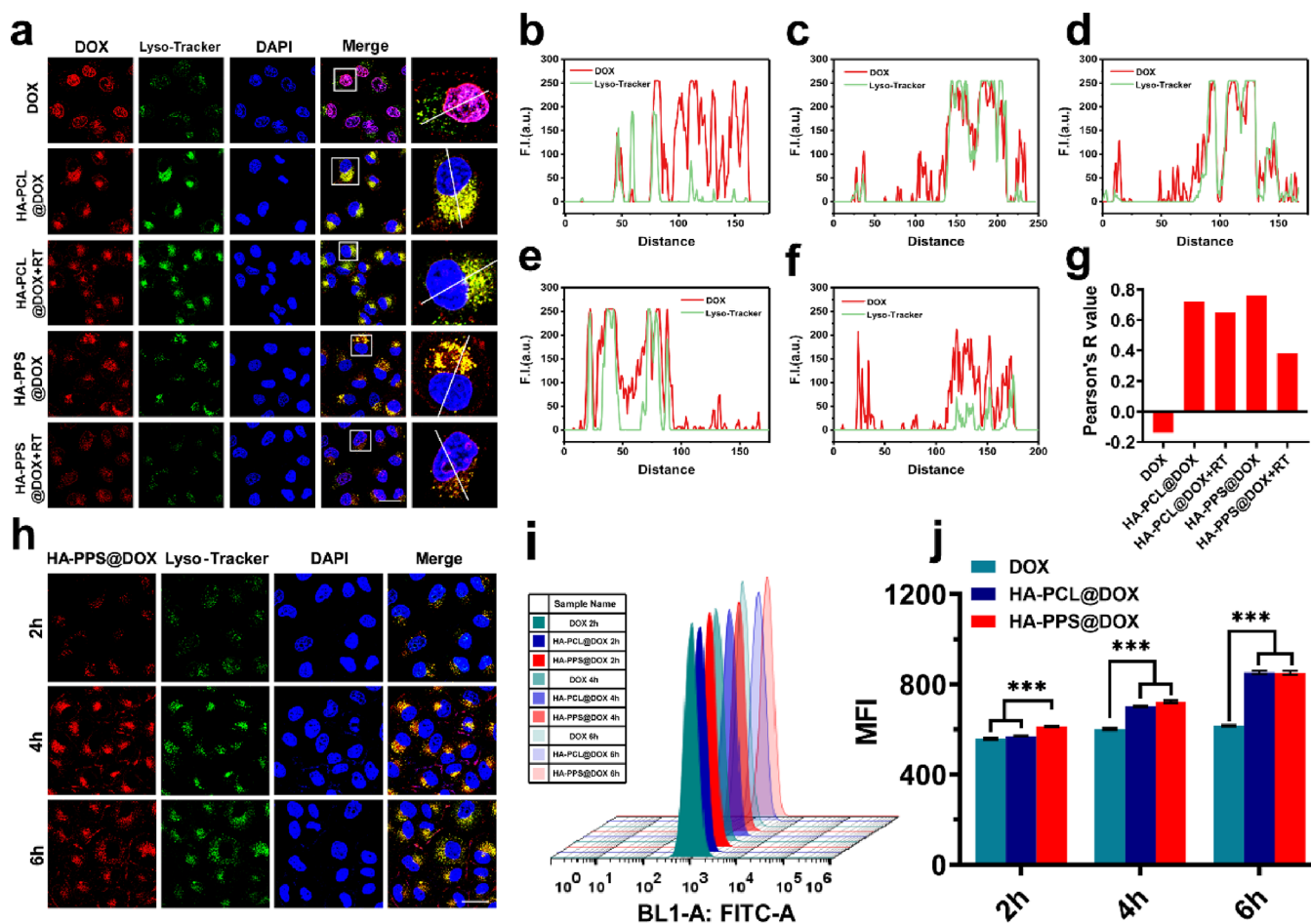


Figure 2. Cellular uptake and cytotoxicity studies of HA-PPS@DOX NMs. (a) Colocalization of DOX formulations with lysosomes. Scale bar: 50 μm . Colocalization curves of lysosomes with free DOX (b), HA-PCL@DOX (c), HA-PCL@DOX+RT (d), HA-PPS@DOX (e), and HA-PPS@DOX+RT (f). (g) Histogram of the colocalization index. (h) CLSM images of HA-PPS@DOX NMs after 2, 4, and 6 h incubation with MCF-7 cells. Scale bar: 50 μm . FCM histograms (i) and quantitative analysis (j) of cellular uptake of free DOX, HA-PCL@DOX, and HA-PPS@DOX after 2, 4, and 6 h incubation. *** $p < 0.001$, data were represented as mean \pm SD ($n = 3$).

disassembly of HA-PPS NMs. Second, the size changes of HA-PPS NMs were evaluated after treatment with γ -ray radiation (8 Gy). As shown in Figure 1g, the homogeneous nanomicelles have broken up into polydisperse particles with varying sizes of 10 nm, 1000 nm, and 10 μm . Furthermore, TEM images showed an obvious morphological change of HA-PPS NMs after radiation, which reflected their ROS-responsive degradation behavior.

Next, in order to study the ROS-responsive drug release behavior of HA-PPS@DOX NMs, the UV-vis absorbance of HA-PPS@DOX NMs was first monitored after incubation with different concentrations of hydrogen peroxide (H_2O_2). As shown in Figure 1h, the UV-vis absorption curve of DOX showed a downward trend as the H_2O_2 concentration increased. Especially in the 2 M H_2O_2 -treated group, the extreme weak absorption peak at 480 nm indicated a sufficient release of DOX due to the disassembly of HA-PPS@DOX NMs, which settled at the bottom of the tube due to their hydrophobic property. Lastly, the ROS-responsive release of DOX from HA-PPS NMs was performed by the dialysis bag method. As described in Figure 1i, after treatment with 1 M H_2O_2 at 37 $^\circ\text{C}$ for 48 h, the accumulative release of DOX achieved 78.01% in HA-PPS@DOX groups, while HA-PPS@DOX without H_2O_2 treatment showed merely 39.66%, which had a significant difference ($p < 0.01$). Additionally, HA-

PCL@DOX NMs (DLC = 20.31%, DLE = 81.24%) with a diameter of approximately 200.13 ± 17.38 nm (Figure S5) were taken as a non-ROS-responsive control. After incubation in the same condition as above, HA-PCL@DOX showed around 34.22 and 33.73% accumulative releases of DOX at 48 h with or without the existence of H_2O_2 , respectively, which showed a significant difference compared with HA-PPS@DOX groups treated with H_2O_2 ($p < 0.01$). These results suggested that H_2O_2 played a slight effect on the release behavior of HA-PCL@DOX NMs while achieving responsive drug release from HA-PPS NMs. Meanwhile, both HA-PPS@DOX NMs and HA-PCL@DOX NMs showed well stability without aggregation or disassembly in water for at least 7 days (Figure S6).

Cellular Uptake and Intracellular Distribution. First, the biocompatibility of the HA-PPS and HA-PCL NMs was evaluated using a CCK-8 kit on L929 mouse fibroblast cells and murine macrophage RAW264.7 cells. As shown in Figure S7a,b, after incubation for 24 h, the survival rates of both L929 cells and RAW264.7 cells were over 90%, which guaranteed better safety of HA-PPS NMs. Subsequently, the hemolysis assay on HA-PPS and HA-PCL NMs was carried out *in vitro*. No obvious hemolysis was observed in these two groups (Figure S8a,b), demonstrating the good biocompatibility of these two nanomicelles.

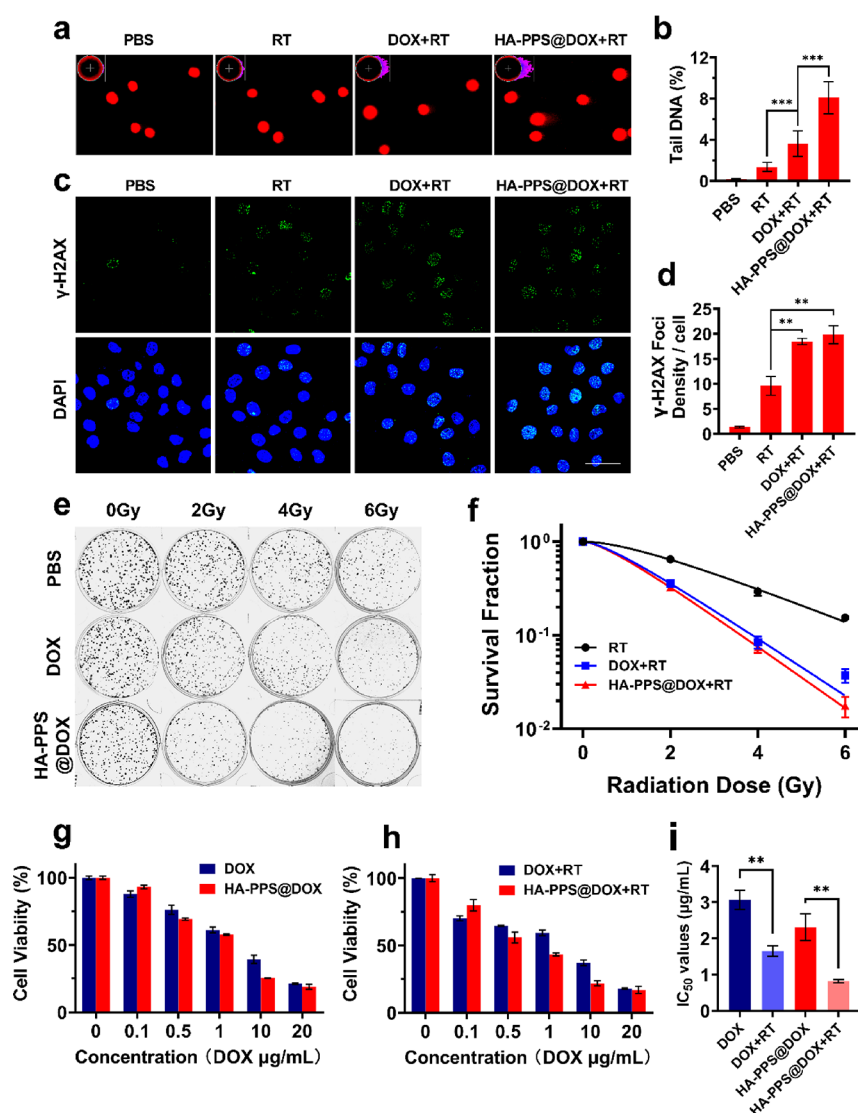


Figure 3. Radiosensitive studies of HA-PPS@DOX NMs. (a) Comet assay of MCF-7 cells treated with PBS, free DOX, and HA-PPS@DOX NMs under 6 Gy radiation using CASP analysis. (b) Tail DNA quantitative analysis of MCF-7 cells treated with PBS, free DOX, and HA-PPS@DOX NMs under 6 Gy radiation. $***p < 0.001$. (c) Immunofluorescence imaging of γ -H2AX foci within MCF-7 cells after treatment with PBS, free DOX, and HA-PPS@DOX NMs under 6 Gy radiation. Scale bar: 50 μm . (d) Quantitative analysis of γ -H2AX foci in MCF-7 cells after treatment with PBS, free DOX, and HA-PPS@DOX NMs under 6 Gy radiation. $**p < 0.01$. (e) Digital images of colony formation treated with PBS, free DOX, and HA-PPS@DOX NMs under 2, 4, and 6 Gy radiation. (f) Colony formation curves of MCF-7 cells treated with PBS, free DOX, and HA-PPS@DOX NMs under 2, 4, and 6 Gy radiation. (g) Cytotoxicity of DOX and HA-PPS@DOX NMs. (h) Cytotoxicity of DOX and HA-PPS@DOX NMs with 8 Gy radiation. Data were expressed as mean \pm SD ($n = 3$). (i) IC_{50} values of two DOX formulations with or without 8 Gy radiation. Data were represented as mean \pm SD ($n = 3$). $**p < 0.01$.

The intracellular distribution was then investigated by the colocalization with lysosomes. After incubation with drugs for 2 h, MCF-7 cells were stained with LysoTracker Red. Apparently, free DOX exhibited the poorest colocalization with lysosomes but mostly clustered in the nucleus (Figure 2a). This is because the free DOX entered cells by the passive diffusion pathway. In contrast, the HA-PPS@DOX and HA-PCL@DOX NMs showed a good fitting with lysosomes, demonstrating that the endocytosis process worked (Figure 2b–f). Next, to quantitatively describe the colocalization of drugs and lysosomes, we calculated Pearson's correlation coefficient through ImageJ software. Compared with non-ROS-responsive HA-PCL@DOX NMs, HA-PPS@DOX NMs exhibited a poor colocalization with lysosomes after γ -ray radiation as demonstrated by the decreased coefficient index of

colocalization (Figure 2g), which might be due to the leakage of DOX from the disassembly of HA-PPS@DOX after radiation.

To study the cellular uptake behavior, the fluorescence colocalization assay of HA-PPS@DOX was carried out after incubating with MCF-7 cells for 2, 4, and 6 h. As shown in Figure 2h, the red fluorescence of DOX gradually intensified over time, which suggested the good uptake of HA-PPS@DOX NMs. Then, the cellular uptake of free DOX, HA-PPS@DOX, and HA-PCL@DOX NMs was further quantitatively analyzed by FCM. Concluded from Figure 2i,j, the internalization behavior of HA-PPS@DOX increased over time as quantified by the mean fluorescence intensities (MFIs). In addition, compared with the free DOX group, much more DOX was endocytosed in HA-PPS@DOX and HA-PCL@DOX groups,

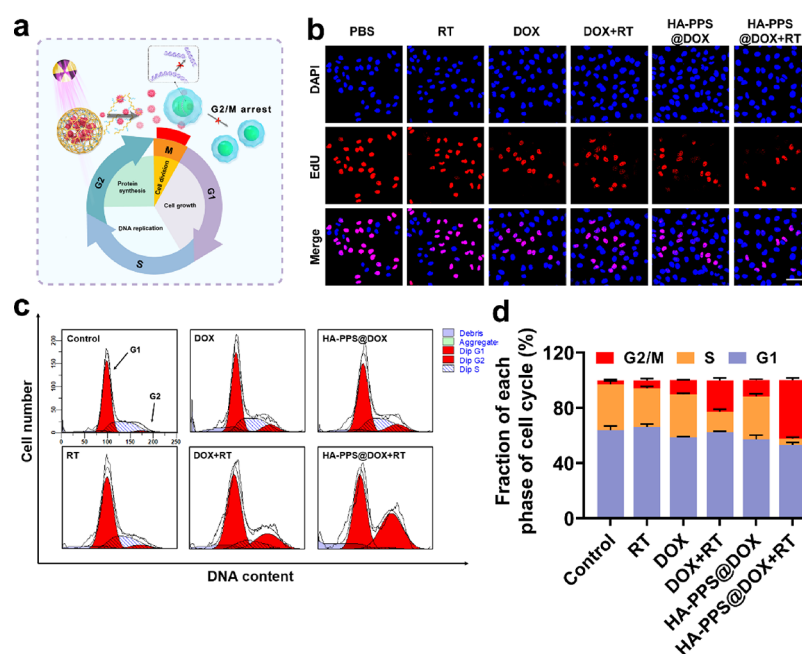


Figure 4. Radiosensitive mechanism of HA-PPS@DOX NMs. (a) Schematic illustration of the radiosensitive mechanism of HA-PPS@DOX NMs. (b) EdU staining of MCF-7 cells treated with PBS, free DOX, and HA-PPS@DOX NMs with or without 6 Gy radiation. Scale bar: 50 μm . (c) Cell cycle assay of MCF-7 cells treated with PBS, free DOX, and HA-PPS@DOX NMs with or without 6 Gy radiation. (d) Quantitative analysis of the cell cycle distribution of MCF-7 cells treated with PBS, free DOX, and HA-PPS@DOX NMs with or without 6 Gy radiation. Data were represented as mean \pm SD ($n = 3$).

illustrating that HA-PPS NMs could enhance the uptake of free DOX, which was attributed to its endocytosis pathway of entering cells.

Radio-Sensitivity Study. DOX is an important chemotherapeutic drug for tumor treatment, which displays its toxic effects through inserting into the DNA strands and inhibiting the topoisomerase II, thereby preventing replication of broken DNA strands.⁴² Therefore, DOX may further enhance radiotherapeutic efficiency by inhibiting the repair of damaged DNA caused by radiotherapy, which enable it to be a potential chemical radiosensitizer. To assess the radiosensitization efficacy of HA-PPS@DOX NMs, DNA double-strand breakage was detected through the comet assay first. As evidenced by the increased percentage of DNA tails (Figure 3a,b) in free DOX and HA-PPS@DOX groups, it could be confirmed that the DNA was seriously damaged, and DOX could reinforce DNA damage caused by radiation for its radiosensitive capacity. More importantly, benefited from the enhanced cellular uptake, HA-PPS@DOX induced more serious breakage of DNA under γ -ray radiation than that of free DOX. Consistently, the much more γ -H2AX foci, a biomarker of DNA double-strand breakage, were shown in the cell nuclei of the HA-PPS@DOX with RT group (Figure 3c,d), further confirming the enhancement of the radio-sensitivity effect. Next, we investigated the inhibition on single-cell colony formation caused by DNA damage. As revealed in Figure 3e, HA-PPS@DOX successfully suppressed the proliferation of cancer cells with an SER value of 1.78, which was superior to that of free DOX (1.66), exhibiting great promise for chemical radiosensitizers (Figure 3f). Finally, the radio-sensitization efficacy was investigated *in vivo*. After treatment, tumor tissues were harvested, and the tumor sections were stained with a γ -H2AX antibody, as shown in Figure S9; much more repair proteins (γ -H2AX foci) were expressed in the HA-PPS@DOX

group than those of free DOX, indicating severe DNA damage and its radio-sensitization efficacy on solid tumors.

Lastly, to explore the antitumor effect caused by chemoradiation therapy, the cytotoxicity of HA-PPS@DOX NMs was measured by the MTT assay. As shown in Figure 3g, in the nonradiation groups, it was found that free DOX did not exhibit more obvious cytotoxicity than HA-PPS@DOX NMs groups, which might be attributed to its poor water solubility. Meanwhile, the HA-PPS@DOX NMs exerted an enhanced therapeutic efficacy, which was benefited from the improved cellular uptake capacity. Afterward, the cytotoxicity of concurrent chemoradiation therapy was evaluated. The cytotoxicities of these two DOX formulations combined with 8 Gy radiation were obviously improved compared to those of single chemotherapy groups, as their IC_{50} values decreased significantly after radiation (Figure 3h,i), showing the superiority of combination therapy. Especially, the IC_{50} value of HA-PPS@DOX has declined to 64.44% from 2.316 to 0.8235 $\mu\text{g}/\text{mL}$, which is superior to that of free DOX (46.16%). All these results demonstrated that the combination therapy achieved a strengthened antitumor effect.

To further investigate the radiosensitive mechanism induced by DOX, an EdU cell proliferation assay was employed to evaluate the inhibition on DNA replication (Figure 4a). EdU (5-ethynyl-2'-deoxyuridine), a thymine nucleoside analogue, can replace thymine (T) to infiltrate into the DNA molecule being replicated in the cell proliferation period and rapidly detect the DNA replication activity through the specific reaction based on EdU and an Apollo fluorescent dye. As shown in Figure 4b, cells treated with all DOX formulations including DOX, DOX+RT, HA-PPS@DOX, and HA-PPS@DOX+RT showed reduced red fluorescence spots compared with PBS groups, which confirmed the inhibited DNA replication capacity. Moreover, the HA-PPS@DOX+RT treatment group presented a better inhibition effect than the HA-

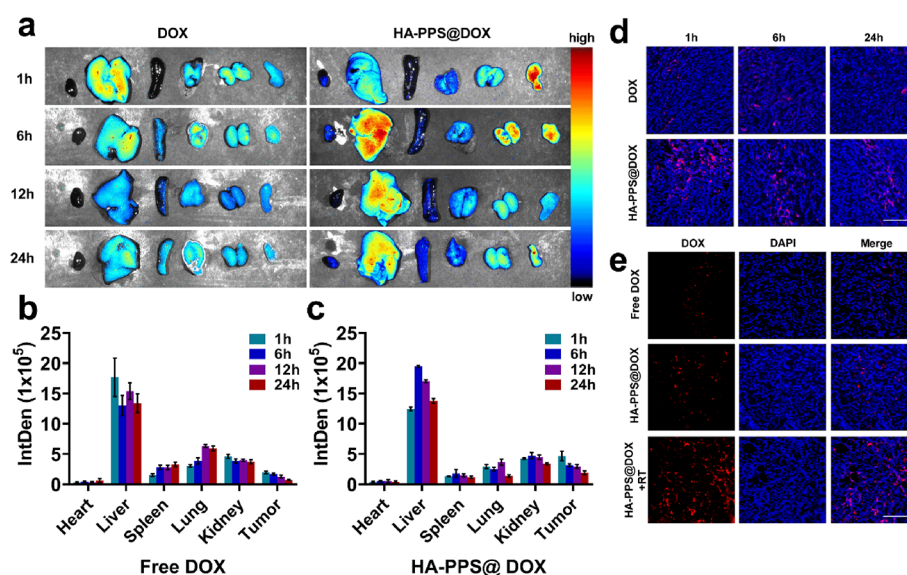


Figure 5. Tissue distribution and tumor accumulation of HA-PPS@DOX NMs. (a) Tissue distribution of DOX and HA-PPS@DOX NMs after 1, 6, 12, and 24 h injection (the tissues are the heart, liver, spleen, lung, kidney, and tumor from left to right). Quantitative detection of DOX (b) and HA-PPS@DOX NMs (c) in the main organs and tumors after 1, 6, 12, and 24 h injection. Data were represented as mean \pm SD ($n = 3$). (d) Tumor accumulation and retention of DOX and HA-PPS@DOX NMs after 1, 6, and 24 h injection. Scale bar: 75 μ m. (e) Drug release behavior of HA-PPS@DOX NMs within tumor tissues with or without γ -ray radiation. Scale bar: 75 μ m.

PPS@DOX group, which was attributed to the ROS-responsive release of DOX from HA-PPS NMs. Meanwhile, cells in different phases exhibited varying degrees of sensitivity to radiotherapy. Generally, the G2/M phase is the most sensitive to radiation, while the S phase is radio-resistant.⁴³ DNA damage mediated by DOX would be followed with cell cycle arrest. To detect the cell cycle change, MCF-7 cells were treated with drugs for 4 h followed by radiation; then, a flow cytometry assay was employed. As the results of Figure 4c conveyed, compared with the control group, single radiotherapy (6 Gy) has little impact on G2/M phase arrest; additionally, cells treated with DOX or HA-PPS@DOX could increase the proportion of the G2/M phase but not significantly. Encouragingly, when radiotherapy was applied along with DOX formulations, there was a prominent increase in the G2/M phase; especially in HA-PPS@DOX+RT groups, the G2/M phase accounted for over 40% of the cell cycle, while the percentage of the S phase had dropped sharply, enabling cells to be more sensitive to radiation.

Biodistribution and Tumor Accumulation of HA-PPS@DOX NMs. Before the animal experiment, *in vivo* biosafety of HA-PPS NMs was first evaluated through hematology analysis and pathological analysis. In brief, being administered with PBS and HA-PPS NMs (two different doses of 15 and 30 mg/kg, respectively), blood biochemistry and hematology of mice were tested after 24 h *i.v.* injection. As a result, the hematology results (WBC, RBC, HGB, HCT, MCV, MCH, MCHC, and PLT) and blood biochemistry indicators (ALB, ALP, ALT, AST, BUN, TBIL, CRE, TP, and UA) entirely ranged within a normal level compared with the PBS group (Figures S10 and S11). Lastly, no obvious inflammation and damage could be found in tissues (heart, liver, spleen, lung, and kidney) by H&E staining (Figure S12). All these results informed us on the negligible side effects of HA-PPS NMs.

Selective accumulation of HA-PPS@DOX in tumor sites is vital for improving drug availability and reducing side effects. Therefore, the time-dependent distribution of HA-PPS@DOX

and free DOX in the main organs of tumor-bearing mice (including the heart, liver, spleen, lung, kidney, and tumor) was monitored by *in vivo* fluorescence imaging. As revealed in Figure 5a,b, free DOX suffered a rapid renal clearance after only 1 h injection, leading to a decreased retention of DOX in the liver and poor tumor accumulation after 24 h injection. On the contrary, in the HA-PPS@DOX group, DOX fluorescence in the liver and kidney achieved its peak concentration after 6 h injection and metabolized gradually as time passed (Figure 5a,c), indicating a longer blood circulation than that of free DOX, which offered it more opportunities to accumulate in tumors. In general, both of these two drugs achieved the highest accumulative level in tumor tissues in 1 h. A more inspiring phenomenon was that the accumulation of HA-PPS@DOX increased, and the tumor retention time had prolonged, which could even extend to 24 h, indicating great potential for long-term curative effects.

Next, the tumor accumulation behaviors were investigated through tissue section analysis by harvesting the tumors at different time points. By comparing fluorescence intensities, we found that the accumulations of free DOX in tumor tissues were all less than those of HA-PPS@DOX after the injection of 1, 6, and 24 h (Figure 5d) since DOX is a small molecule that is easy to be cleared during blood circulation, thus leading to the inefficient tumor accumulation of free DOX. In contrast, the synthetic HA-PPS@DOX NMs could largely accumulate around the tumor tissues through the EPR effect for their appropriate size. This has been proven by the phenomenon that there was still a strong red fluorescence intensity after 24 h injection in the HA-PPS@DOX treatment group, while in the DOX group, almost no fluorescence signal of DOX could be captured at 24 h (Figure 5d).

Then, the feasibility of the ROS-responsive drug release process *in vivo* was investigated. After being injected with DOX or HA-PPS@DOX for 1 h, the tumor-bearing mice received a local radiation (8 Gy) treatment. Then, the tumor tissues were excised for drug release investigation 1 h later. Obviously,

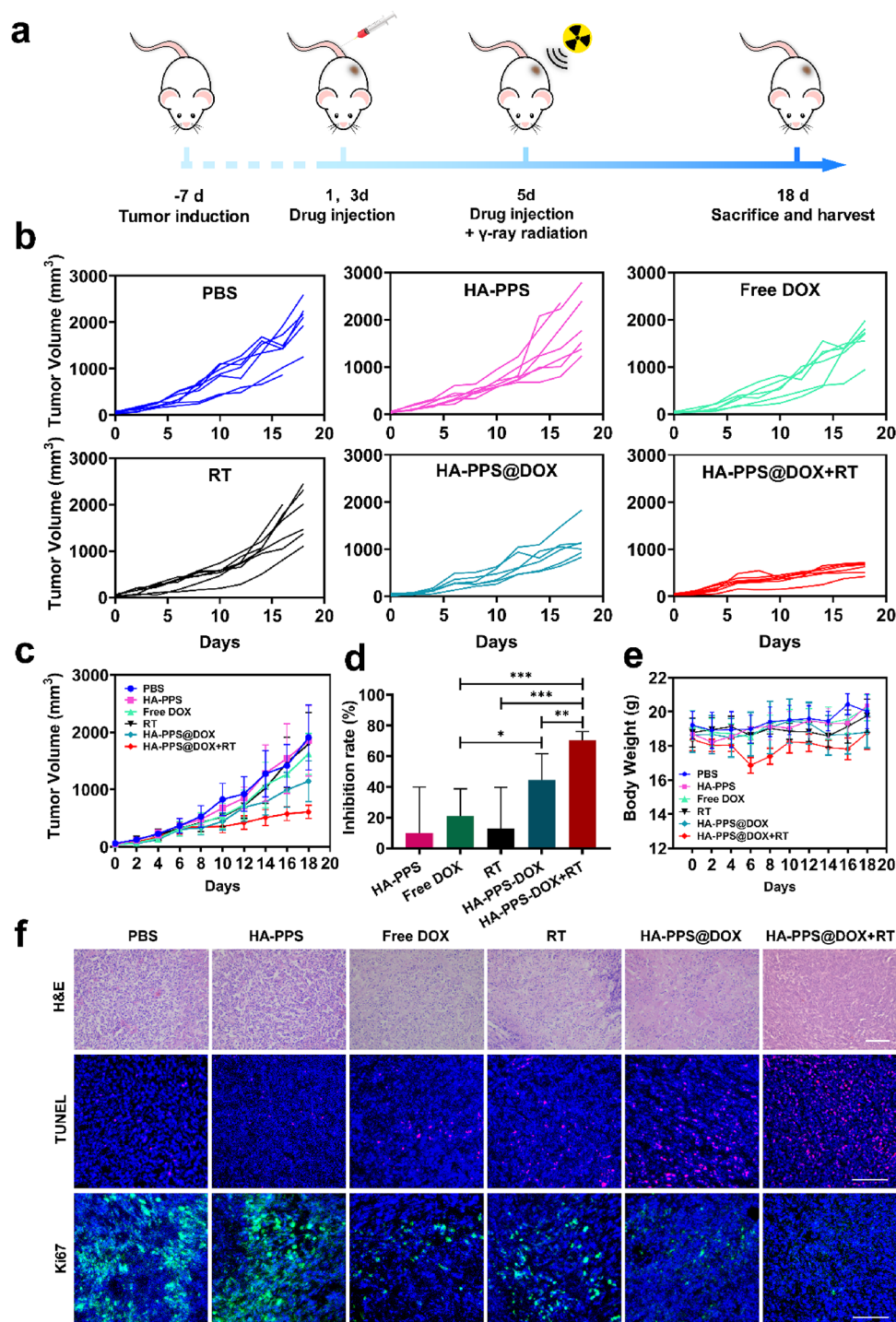


Figure 6. *In vivo* antitumor study. (a) Schedule of concurrent chemoradiation therapy. (b) Tumor volume curves of individual animals treated with PBS, HA-PPS NMs, free DOX, RT, HA-PPS@DOX NMs, and HA-PPS@DOX NMs combined with RT. (c) Overall tumor growth curves from different kinds of treatment groups. (d) Tumor inhibition rate of different kinds of treatment groups. * $p < 0.05$. ** $p < 0.01$. *** $p < 0.001$. (e) Body weight of different kinds of treatment groups during 18 days of treatment. (f) Pathological analysis (scale bar of 200 μm) and immunofluorescence analysis (TUNEL and Ki67 staining, scale bar of 75 μm) of tumor tissues from different kinds of treatment groups. Data were expressed as mean \pm SD ($n = 7$).

compared with the HA-PPS@DOX group, the HA-PPS@DOX with RT group exhibited a brighter fluorescence signal emitted by DOX (Figure 5e), proving that much more DOX had released from HA-PPS@DOX triggered by radiation. Generally speaking, HA-PPS@DOX NMs enabled DOX a favorable ability to accumulate in tumor sites; the enhanced

accumulation combined with the responsive release process synergistically increased the drug delivery efficiency.

***In Vivo* Antitumor Efficacy.** Given the encouraging anticancer results *in vitro*, the *in vivo* antitumor studies were carried out using 4T1 tumor-bearing BALB/c mice, which were *i.v.* administered with HA-PPS@DOX (at equivalent DOX doses of 4 mg/kg mouse weight) followed by γ -ray

irradiation (8 Gy) 1 h later. The 4T1 tumor model was established, and the tumor therapy was carried out according to the scheme shown in Figure 6a. As shown in Figure 6b,c, compared with the control group, treatment with HA-PPS NMs almost could not restrain the tumor growth. Groups of free DOX or RT had a quite limited effect on tumor inhibition, which reflected the unsatisfactory treatment outcomes by a single therapy. In addition, despite HA-PPS@DOX turning out to be a relatively good therapeutic effect, it merely achieved a 44.3% growth inhibition rate. Comparatively, as treatment of HA-PPS@DOX accompanied with RT was performed, the inhibition rate even reached to 70.4%, which was noticeably in excess of other treatment groups (Figure 6d), reflecting a significant synergistic antitumor efficacy of our combination therapy. Additionally, the body weights of mice in all groups basically fluctuated within a narrow range during the therapeutic period (Figure 6e). After treatments, the main organs of mice in all groups were taken for pathological analysis, and no apparent harm occurred (Figure S13), which confirmed the biosafety of such a drug delivery platform.

In the end of the treatment, all mice were sacrificed, and the harvested tumors were processed for apoptosis, proliferation, and histological analysis. Indicated by the H&E staining results (Figure 6f), different degrees of histopathological changes were discovered in free DOX, RT, and HA-PPS@DOX treatment groups; noticeably, there was the most serious necrosis in HA-PPS@DOX with the RT treatment group. Based on H&E results, research studies on cell apoptosis and proliferation were performed for an in-depth investigation. As Figure 6f exhibits, in the HA-PPS@DOX with RT treatment group, the significant intensive red fluorescence dots representing the apoptotic DNA detected by the TUNEL assay indicated obvious apoptosis of tumor tissues compared with other groups. Subsequently, Ki67, a biomarker of cell proliferation, was employed to mark the tumor growth. It was obvious that the tumor tissues multiplied vigorously in the control group, but by contrast, the tumor proliferation suffered an effective limit in light of the almost invisible Ki67 fluorescence signal when HA-PPS@DOX with RT treatment was used. Therefore, there was sufficient evidence suggesting that our combination strategy indeed provided a promising therapy for cancer treatment.

EXPERIMENTAL SECTION

Materials. Hyaluronic acid, propylene sulfide, adipic dihydrazide, caprolactone, *N*-Boc-ethanolamine, doxorubicin hydrochloride (DOX·HCl), dicyclohexylcarbodiimide (DCC), 4-dimethylaminopyridine (DMAP), ethyl-3-(3-dimethylaminopropyl) carbodiimidehydrochloride (EDC·HCl), and *N*-hydroxysuccinimide (NHS) were purchased from Sigma-Aldrich Co., Ltd. (Beijing, China). *N,N*-Dimethylformamide (DMF) and triethylamine (TEA) were purchased from Alfa Aesar Co., Ltd. (Shanghai, China). 2,7-Dichlorofluorescein diacetate (DCFH-DA) was purchased from Yeasen Biotechnology Co., Ltd. (Shanghai, China). 4',6-Diamidino-2-phenylindole (DAPI), propidium iodide (PI), 3-(4,5-dimethylthiazol-2-yl)-2,5-diphenyltetrazolium bromide (MTT), and TUNEL agents were obtained from Solarbio Co., Ltd. (Beijing, China). Cell culture agents were purchased from GIBCO. Antibodies were acquired from Abcam Co., Ltd. (Shanghai, China).

Synthesis of Poly(propylene sulfide) (PPS). According to the previous study,⁴⁴ *S*-methyl thioacetate (1 equiv) was dissolved in 2 mL of THF and reacted with sodium methoxide

(1.05 equiv) for 30 min under the protection of nitrogen at room temperature. Next, propylene sulfide (27 equiv) was added into the mixture and then reacted for 6 h at 65 °C, which also needed a protection of nitrogen. Afterward, 3-bromopropionic acid was introduced as a capping agent. The structure was characterized by ¹H nuclear magnetic resonance (¹H NMR) (Bruker, AVANCE III HD 300 MHz) and Fourier infrared spectrometry (FTIR) (Thermo Scientific Nicolet iS10).

Synthesis of HA-PPS. First, hyaluronan was modified with adipic dihydrazide. In brief, hyaluronan (1 g) was dissolved in water and activated by EDC/NHS for 30 min. Then, adipic dihydrazide (2.2 g) was added to the above solution and reacted for 24 h at room temperature. Subsequently, the product was purified by adequate dialysis against distilled water (MWCO = 3500 Da), and finally, the HA-AD was obtained after lyophilization.

Second, the HA-PPS polymer was synthesized with HA-AD and PPS at a mass ratio of 3:1. Briefly, HA-AD (600 mg) and PPS (200 mg) were dissolved in 20 mL of DMSO, added with DCC/DMAP as a catalyst. Stirred for 48 h at room temperature, the mixture solution was purified by adequate dialysis against distilled water (MWCO = 3500 Da) for 2 days. Finally, HA-PPS powder was acquired by lyophilizing the aqueous solution. The structure was characterized by ¹H NMR (Bruker, AVANCE III HD 300 MHz) and FTIR (Thermo Scientific Nicolet iS10).

Polycaprolactone (PCL) was synthesized through ring-opening polymerization according to a previous study.³⁵ Then, HA-PCL polymers were synthesized with HA and PCL at a mass ratio of 4:1. HA (500 mg) and PCL (125 mg) were used as a conjugated method of HA-PPS. The structure was characterized by ¹H NMR (Bruker, AVANCE III HD 300 MHz).

Preparation and Characterization of HA-PPS NMs. HA-PPS or HA-PCL polymers were dissolved in the mixture of DMF and water; then, the solution was sonicated with an Ultrasonic Cell Disruptor for 5 min (20 W, 10 s on, 5 s off, 40%). After stirring for 2 h, the solution was dialyzed in ultrapure water (MWCO = 3500 Da) for 24 h to remove DMF then centrifuged under 3000 rpm for 5 min to remove the precipitates, and eventually, the polymer nanomicelle solution was acquired. The hydrodynamic size and morphology were characterized using a dynamic light scatterer (DLS) (Brookhaven, Omni) and a transmission electron microscope (TEM) (JEM-2100F). To confirm the γ -ray-triggered disassembly of HA-PPS NMs, their hydrodynamic size and morphology were characterized using a DLS and a TEM after radiation (8 Gy).

Preparation and Characterization of HA-PPS@DOX NMs. DOX·HCl (2 mg) was dissolved in DMF (4 mL) and solubilized upon the addition of triethylamine (2 μ L). After stirring for 2 h, the mixture containing hydrophobic free DOX was added into the prepared polymer nanomicelles dropwise and stirred for another 24 h. Next, the solution was dialyzed in ultrapure water (MWCO = 3500 Da) to remove DMF, triethylamine, and extra DOX·HCl; the free DOX was then enclosed in the core of nanomicelles through hydrophobic interaction. The hydrodynamic size and morphology of HA-PPS@DOX or HA-PCL@DOX were characterized using a DLS (Brookhaven, Omni) and a TEM (JEM-2100F). Then UV–visible spectra of HA-PPS@DOX or HA-PCL@DOX were measured to calculate the DOX concentration according

to the standard curve of DOX absorption at 480 nm (ranging from 10 to 500 $\mu\text{g}/\text{mL}$, $R^2 = 0.999$). The drug loading content (DLC) and drug loading efficiency (DLE) of DOX were defined according the following equations: DLC (%) =

$$\frac{\text{Mass of loaded DOX}}{\text{Mass of DOX} - \text{loaded nanomicelles}} \times 100\% \quad (1)$$

DLE (%) =

$$\frac{\text{Mass of loaded DOX}}{\text{Mass of added DOX}} \times 100\% \quad (2)$$

To evaluate the leakage of DOX from nanomicelles, HA-PPS@DOX NMs were incubated with different concentrations of H_2O_2 for 6 h; then, the mixture solution was centrifuged, and the ultraviolet absorption of the supernatant was measured at 480 nm. Additionally, to measure the drug release curve, HA-PPS@DOX and HA-PCL@DOX micelles were incubated in PBS (0.1 M, pH 7.4) with or without H_2O_2 (1 M) at 37 $^\circ\text{C}$. The release behavior of DOX was studied by measuring the absorbance of the dialysate at 480 nm during different time points.

Biocompatibility and Cytotoxicity Assay *In Vitro*.

Human breast cancer cells (MCF-7) and L929 mouse fibroblast cells (L929) were incubated with a DMEM medium including 10% fetal bovine serum (FBS), penicillin (100 U/mL), and streptomycin (100 mg/mL). Murine macrophage RAW264.7 cells were cultured in the same condition but with an RPMI 1640 medium. All cells were kept in an atmosphere of 5% CO_2 at 37 $^\circ\text{C}$.

To evaluate the biocompatibility of HA-PPS and HA-PCL, L929 cells or murine macrophage RAW264.7 cells were seeded in a 96-well plate at a density of 1×10^4 cells/well. After 24 h incubation at 37 $^\circ\text{C}$, HA-PPS and HA-PCL NMs were added with various concentrations and further cocultured for 24 h. Afterward, the culture solution was removed and replaced with 100 μL of a fresh medium containing 10 μL of a CCK-8 reagent for each well followed by 2 h incubation. Its OD value was detected at a wavelength of 450 nm using a multifunctional enzyme marker. In addition, the *in vitro* hemolysis assay was employed. According to a previous study,⁴⁶ 500 μL of a mouse red blood cell suspension was incubated with HA-PPS and HA-PCL NMs in different concentrations at 37 $^\circ\text{C}$ for 3 h. Then, the mixture was centrifuged, and digital images were recorded. Subsequently, 100 μL of the supernatant was taken for optical absorbance detection at 570 nm. Finally, the hemolysis ratio was calculated.

To evaluate the cytotoxicity of HA-PPS@DOX and free DOX (refer to hydrophobic DOX), MCF-7 cells were seeded in a 96-well plate at a density of 1×10^4 cells/well and incubated for 24 h. Afterward, HA-PPS@DOX and free DOX were added to each well in different concentrations. With another 24 h incubation, a cell viability assay was performed by the methyl thiazolyl tetrazolium (MTT) method. For the chemoradiation study, HA-PPS@DOX and free DOX were added to each well in different concentrations followed by γ -ray radiation in a dose of 8 Gy 24 h later. With another 24 h incubation, cell viability was evaluated by an MTT assay.

Cellular Uptake Study. MCF-7 cells were seeded in 6-well plates at a density of 2×10^5 cells/well. Twenty-four hours later, the medium was replaced by HA-PPS@DOX, HA-PCL@DOX, and free DOX medium solution (2 $\mu\text{g}/\text{mL}$ of DOX equivalents) and further cocultured with cells for 2, 4, and 6 h. Soon after, all cells were washed with PBS (pH 7.4) and

trypsinized then resuspended in PBS for the detection of DOX fluorescence signals by flow cytometry (FCM). In addition, for a fluorometric analysis, MCF-7 cells were fixed with 4% paraformaldehyde for 30 min after treatment with HA-PPS@DOX for 2, 4, and 6 h and then stained with DAPI. Lastly, the cells were observed under confocal laser scanning microscopy (CLSM).

Intracellular Distribution Study. MCF-7 cells were cultured in confocal dishes at a density of 1.5×10^5 cells/dish for 24 h followed by 2 h incubation with HA-PPS@DOX, HA-PCL@DOX, and free DOX medium solution (2 $\mu\text{g}/\text{mL}$ of DOX equivalents). Afterward, γ -ray radiation (8 Gy) was applied followed by a further incubation of 2 h. To demonstrate the intracellular distribution of drugs in cells, LysoTracker Red was used to observe its colocalization with DOX. Briefly, the cells were washed with PBS before LysoTracker Red staining. Being fixed with 4% paraformaldehyde, the cells were stained with DAPI. Ultimately, fluorescence was observed under CLSM.

Intracellular ROS Measurement. Confocal dishes were seeded with MCF-7 cells for 1.5×10^5 cells/dish. After 24 h, the medium was replaced by a fresh medium containing HA-PPS (100 $\mu\text{g}/\text{mL}$) and HA-PCL (100 $\mu\text{g}/\text{mL}$). After 2 h incubation, a DCFH-DA probe (1×10^{-5} M) was added and cocultured with cells for 20 min. Incubated for 30 min after the γ -ray radiation (8 Gy), all cells were observed under CLSM.

Immunostaining Assay of DNA Double-Strand Break.

MCF-7 cells were seeded in confocal dishes at a density of 1.5×10^5 cells/dish for 24 h incubation then replaced with a medium containing HA-PPS@DOX and free DOX (2 $\mu\text{g}/\text{mL}$ of DOX equivalents). γ -Ray radiation (4 Gy) was conducted 4 h later with a further incubation of 1 h. Subsequently, cells were permeabilized with 0.5% Triton X-100 for 15 min and then blocked in 1% bovine serum albumin (BSA) for 1 h after being fixed with 4% paraformaldehyde. Then, cells were incubated with a mouse anti-gamma γ -H2AX antibody at 4 $^\circ\text{C}$ overnight. After being washed with PBS, cells were incubated with an Alexa Fluor 488 conjugated rabbit antimouse secondary antibody for 1 h at room temperature followed by DAPI staining. The γ -H2AX foci were observed under CLSM.

Clone Formation Assay. MCF-7 cells were seeded in 6-well plates at a density of 1×10^3 cells/well. After 24 h, the medium was replaced with a fresh medium, HA-PPS@DOX, and free DOX (2 $\mu\text{g}/\text{mL}$ of DOX equivalents) solution for 24 h incubation. All wells were replaced with a fresh medium and irradiated under γ -rays at doses of 0, 2, 4, and 6 Gy. After 7 days of incubation, the visible cell clusters were stained with crystal violet. The clone plate was washed softly and dried in air for calculation of the clone foci. The sensitization enhancement ratio was determined by a multitarget single-hit model as that in a previous study.⁴⁷

Comet Assay. DNA breakage was detected by single-cell gel electrophoresis. Briefly, MCF-7 cells were seeded in 6-well plates at a density of 2×10^5 cells/well for 24 h followed by 2 h incubation with a fresh medium containing HA-PPS@DOX and free DOX (2 $\mu\text{g}/\text{mL}$ of DOX equivalents). Being irradiated by γ -rays at a dose of 4 Gy, the cells were collected and resuspended in PBS at a density of 1×10^6 cells/mL. A 30 μL single-cell suspension was taken and mixed with 70 μL of low-melting-point agarose then spread equally upon the agarose on microscope slides. Afterward, the slides were immersed in the cell lysis buffer for 2.5 h and in the electrophoretic liquids for 20 min; then, electrophoresis at 30

V was adopted. Being neutralized for 20 min, the slides were washed with PBS, and the comets were stained with Gel-Red. Images were captured by fluorescence microscopy, and DNA damage was analyzed with the comet assay software project (CASP).

Cell Proliferation Assay. MCF-7 cells were seeded and incubated in confocal dishes at a density of 1.5×10^5 cells/dish overnight. Then, cells were incubated with a fresh medium, free DOX, and HA-PPS@DOX for 4 h followed by γ -ray radiation (8 Gy). After 1 h incubation, EdU agents were added and coincubated with cells for 2 h at 37 °C. Afterward, cells were fixed with 4% paraformaldehyde and permeabilized with 0.5% Triton X-100 for 15 min. Being washed with PBS for three times, cells were stained with an Apollo dye and Hoechst33342 successively. Finally, fluorescence was observed under CLSM.

Cell Cycle Assay. MCF-7 cells were seeded in 6-well plates at a density of 2×10^5 cells/well for 24 h. Then, cells were incubated with a fresh medium, HA-PPS@DOX, or free DOX (0.2 μ g/mL of DOX equivalents) for 4 h. After γ -ray radiation (6 Gy), cells were collected and resuspended in PBS followed by the fixation with 70% ice ethyl alcohol overnight in 4 °C. Being washed with PBS, cells were stained with PI working solution for 30 min under 37 °C, and the PI signal was detected by flow cytometry (FCM) at once.

Safety Evaluation In Vivo. To evaluate the *in vivo* safety, HA-PPS was injected (two different doses of 15 and 30 mg/kg) through the tail vein. Whole blood was derived from the ocular vein of mice after 24 h injection. The blood routine index and the blood biochemical index were analyzed through the obtained serum. In addition, the obtained organs including the heart, liver, spleen, lung, and kidney were fixed and made as a paraffin section for H&E staining.

Tissue Biodistribution and Tumor Accumulation Study. Female BALB/c nude mice (4–6 weeks old) were purchased from Beijing Vital River Laboratory Animal Technology Co., Ltd. and kept in a specific pathogen-free (SPF) environment. All animal experiments were performed strictly under the guidelines of the Institutional Animal Care and Use Committee of China. 4T1 cells (2×10^6) suspended in 100 μ L of PBS (pH 7.4) were subcutaneously injected into the right armpit of each mouse.

The mice were sacrificed at 1, 6, 12, and 24 h after intravenous injection with free DOX and HA-PPS@DOX ($n = 3$). Then, the main organs or tissues containing the heart, liver, spleen, lung, kidney, and tumor were collected for the measurement of DOX fluorescence intensity using a non-invasive optical imaging system (IVIS) spectrum small-animal imaging system.

The tumor retention of HA-PPS@DOX was also studied via fluorescence imaging of tumor slides. The harvested tumors at different time points were quickly frozen in liquid nitrogen and embedded in an OCT compound; then, they were made into frozen slices on a cryostat microtome. Subsequently, the frozen slices were immersed in PBS for 1 min to remove the embedding medium and sealed with a mounting medium, which contained DAPI. Finally, the images of DOX and DAPI fluorescence were captured with CLSM, through which we could evaluate the DOX or HA-PPS@DOX tumor penetration capacity.

For γ -H2AX detection, after being injected with PBS, DOX, or HA-PPS@DOX (at equivalent DOX doses of 4 mg/kg mouse weight) for 1 h, 4T1 tumor-bearing mice were

irradiated by γ -rays at a dose of 6 Gy. After 1 h injection, the tumors were harvested and cut into slices. After blocking in 1% BSA for 30 min, the tissue slices were incubated with a mouse antigamma γ -H2AX antibody overnight under 4 °C followed by 2 h incubation of a secondary antibody at room temperature. Finally, the tumor slides were imaged by CLSM after blocking with DAPI.

In Vivo Antitumor Therapy. The tumor-bearing mice were randomly divided into 6 groups ($n = 7$). On day 1, 3, and 5, saline, saline (RT+), HA-PPS, free DOX, HA-PPS@DOX, and HA-PPS@DOX (RT+) were injected through the caudal vein (4 mg/kg of the DOX dose). Then, tumors in “RT+” groups were irradiated by γ -rays at a dose of 8 Gy when mice were injected with drugs 1 h later on day 5. The body weights and tumor volumes (V (mm³) = $ab^2/2$ (a = the longest dimension, b = the shortest dimension)) were recorded every 2 days during treatment. On day 18, all the mice were sacrificed for harvesting the main organs (heart, liver, spleen, lung, and kidney) and tumors, which were perfused and fixed with 4% paraformaldehyde for H&E staining.

For Ki-67 staining, frozen slices were washed with PBS and then blocked by 1% BSA. Being washed with PBS, the tissue slices were incubated with a rabbit anti-Ki67 antibody overnight under 4 °C followed by 2 h incubation of a secondary antibody at room temperature. Finally, the tumor slices were imaged by CLSM after blocking with DAPI.

To detect tumor apoptosis, the prepared slices were incubated with TUNEL working solution for 45 min under 37 °C. The tumor slices were then imaged by CLSM after blocking with DAPI.

Statistical Analysis. Significant differences between two groups were evaluated by unpaired two-tailed *t* tests using GraphPad Prism 8.0 software, and $p < 0.05$, $p < 0.01$, and $***p < 0.001$ were considered as significant differences. Data were presented as mean \pm SD.

CONCLUSIONS

In summary, a DOX-loaded ROS-sensitive nanomicelle was developed to apply for high-efficiency concurrent chemoradiation cancer treatment. Upon γ -ray radiation, HA-PPS@DOX NMs could be oxidized by the generated ROS, triggering the destruction of nanovesicles. Subsequently, the released DOX contributed to enhancement of the cytotoxicity. Meanwhile, as a radio-sensitizer, DOX combined with radiotherapy has dramatically declined the IC₅₀ value from 2.316 to 0.8235 μ g/mL, preliminarily exhibiting an enhanced efficacy of concurrent chemoradiation therapy, which can be further confirmed by the SER value of 1.78. *In vivo* studies found out that benefited from the increased cellular uptake and appropriate size of HA-PPS nanocarriers, both the accumulation amount and retention time of HA-PPS@DOX NMs had been improved compared with free DOX. After *in situ* radiation in tumor sites, DOX was released from HA-PPS NMs and exerted a therapeutic effect with radiotherapy in concert. Consequently, an ideal tumor inhibition rate of 70.4% was achieved by the high-efficiency concurrent chemoradiation cancer therapy, which may provide a reference for clinical cancer treatment.

ASSOCIATED CONTENT

Supporting Information

The Supporting Information is available free of charge at <https://pubs.acs.org/doi/10.1021/acsomega.1c01500>.

Additional figures; synthesis procedure of HA-PPS; ^1H NMR of PPS; UV-vis spectra of free DOX and HA-PPS@DOX NMs; ^1H NMR spectra of PCL and HA-PCL; size distribution of HA-PCL and HA-PCL@DOX NMs; cytotoxicity assay of L929 cells and RAW264.7 cells treated with HA-PCL and HA-PPS NMs; hemolysis photographs and hemolysis percentage; immunofluorescence imaging of $\gamma\text{-H2AX}$ foci within tumor tissues; hematology results; blood biochemistry data; H&E-stained tissue slices (PDF)

AUTHOR INFORMATION

Corresponding Authors

Yumin Zhang – Tianjin Key Laboratory of Radiation Medicine and Molecular Nuclear Medicine, Institute of Radiation Medicine, Chinese Academy of Medical Sciences and Peking Union Medical College, Tianjin 300192, China; Phone: (+86)-022-85682399; Email: zhangyumin@irm-cams.ac.cn

Guoliang Li – Lab of Functional and Biomedical Nanomaterials, College of Materials Science and Engineering, Qingdao University of Science and Technology, Qingdao 266042, China; Phone: (+86)-0532-84022901; Email: ligl@qust.edu.cn

Jianfeng Liu – Lab of Functional and Biomedical Nanomaterials, College of Materials Science and Engineering, Qingdao University of Science and Technology, Qingdao 266042, China; Tianjin Key Laboratory of Radiation Medicine and Molecular Nuclear Medicine, Institute of Radiation Medicine, Chinese Academy of Medical Sciences and Peking Union Medical College, Tianjin 300192, China; orcid.org/0000-0003-0541-5072; Phone: (+86)-022-85683019; Email: liujianfeng@irm-cams.ac.cn

Authors

Ying Yu – Lab of Functional and Biomedical Nanomaterials, College of Materials Science and Engineering, Qingdao University of Science and Technology, Qingdao 266042, China

Zujian Feng – Department of Polymer Science and Engineering, Key Laboratory of Systems Bioengineering (Ministry of Education), School of Chemical Engineering and Technology, Tianjin University, Tianjin 300072, China

Jinjian Liu – Tianjin Key Laboratory of Radiation Medicine and Molecular Nuclear Medicine, Institute of Radiation Medicine, Chinese Academy of Medical Sciences and Peking Union Medical College, Tianjin 300192, China; orcid.org/0000-0001-5176-7613

Xiaoxue Hou – Tianjin Key Laboratory of Radiation Medicine and Molecular Nuclear Medicine, Institute of Radiation Medicine, Chinese Academy of Medical Sciences and Peking Union Medical College, Tianjin 300192, China

Xiaoqian Zhou – Lab of Functional and Biomedical Nanomaterials, College of Materials Science and Engineering, Qingdao University of Science and Technology, Qingdao 266042, China

Jie Gao – Tianjin Key Laboratory of Radiation Medicine and Molecular Nuclear Medicine, Institute of Radiation Medicine, Chinese Academy of Medical Sciences and Peking Union Medical College, Tianjin 300192, China

Wei Wang – Lab of Functional and Biomedical Nanomaterials, College of Materials Science and Engineering,

Qingdao University of Science and Technology, Qingdao 266042, China; orcid.org/0000-0002-7762-7560

Complete contact information is available at: <https://pubs.acs.org/10.1021/acsomega.1c01500>

Notes

The authors declare no competing financial interest.

ACKNOWLEDGMENTS

This work was supported by the National Natural Science Foundation of China (81971731 and 51703247), the National Science Fund for Distinguished Young Scholars of Tianjin (18JCJQC47300), and the Nonprofit Central Research Institute Fund of the Chinese Academy of Medical Sciences (2018PT35031).

REFERENCES

- (1) Bregni, G.; Akin Telli, T.; Camera, S.; Deleporte, A.; Moretti, L.; Bali, A. M.; Liberale, G.; Holbrechts, S.; Hendlisz, A.; Sclafani, F. Adjuvant Chemotherapy for Rectal Cancer: Current Evidence and Recommendations for Clinical Practice. *Cancer Treat Rev* **2020**, *83*, 101948.
- (2) Wang, Q.; Xiao, M.; Wang, D.; Hou, X.; Gao, J.; Liu, J.; Liu, J. In Situ Supramolecular Self-Assembly of Pt(IV) Prodrug to Conquer Cisplatin Resistance. *Adv. Funct. Mater.* **2021**, 2101826.
- (3) Song, G.; Cheng, L.; Chao, Y.; Yang, K.; Liu, Z. Emerging Nanotechnology and Advanced Materials for Cancer Radiation Therapy. *Adv. Mater.* **2017**, *29*, 1700996.
- (4) Zhang, X. D.; Luo, Z.; Chen, J.; Shen, X.; Song, S.; Sun, Y.; Fan, S.; Fan, F.; Leong, D. T.; Xie, J. Ultrasmall Au (10-12) (SG) (10-12) Nanomolecules for High Tumor Specificity and Cancer Radiotherapy. *Adv. Mater.* **2014**, *26*, 4565–4568.
- (5) Dou, Y.; Guo, Y.; Li, X.; Li, X.; Wang, S.; Wang, L.; Lv, G.; Zhang, X.; Wang, H.; Gong, X.; et al. Size-Tuning Ionization to Optimize Gold Nanoparticles for Simultaneous Enhanced CT Imaging and Radiotherapy. *ACS Nano* **2016**, *10*, 2536–2548.
- (6) Jiang, W.; Li, Q.; Xiao, L.; Dou, J.; Liu, Y.; Yu, W.; Ma, Y.; Li, X.; You, Y. Z.; Tong, Z.; et al. Hierarchical Multiplexing Nanodroplets for Imaging-Guided Cancer Radiotherapy via DNA Damage Enhancement and Concomitant DNA Repair Prevention. *ACS Nano* **2018**, *12*, 5684–5698.
- (7) Zhang, P.; Zhai, Y.; Cai, Y.; Zhao, Y.; Li, Y. Nanomedicine-Based Immunotherapy for the Treatment of Cancer Metastasis. *Adv. Mater.* **2019**, *31*, 1904156.
- (8) Ni, K.; Luo, T.; Culbert, A.; Kaufmann, M.; Jiang, X.; Lin, W. Nanoscale Metal-Organic Framework Co-delivers TLR-7 Agonists and Anti-CD47 Antibodies to Modulate Macrophages and Orchestrate Cancer Immunotherapy. *J. Am. Chem. Soc.* **2020**, *142*, 12579–12584.
- (9) Liu, X.; Feng, Z.; Wang, C.; Su, Q.; Song, H.; Zhang, C.; Huang, P.; Liang, X. J.; Dong, A.; Kong, D.; et al. Co-localized Delivery of Nanomedicine and Nanovaccine Augments the Postoperative Cancer Immunotherapy by Amplifying T-cell Responses. *Biomaterials* **2020**, *230*, 119649.
- (10) Xiao, H.; Guo, Y.; Li, B.; Li, X.; Wang, Y.; Han, S.; Cheng, D.; Shuai, X. M2-Like Tumor-Associated Macrophage-Targeted Codelivery of STAT6 Inhibitor and IKK β siRNA Induces M2-to-M1 Repolarization for Cancer Immunotherapy with Low Immune Side Effects. *ACS Cent. Sci.* **2020**, *6*, 1208–1222.
- (11) Roma-Rodrigues, C.; Rivas-Garcia, L.; Baptista, P. V.; Fernandes, A. R. Gene Therapy in Cancer Treatment: Why Go Nano? *Pharmaceutics* **2020**, *12*, 233.
- (12) Zhou, J.; Wu, Y.; Wang, C.; Cheng, Q.; Han, S.; Wang, X.; Zhang, J.; Deng, L.; Zhao, D.; Du, L.; et al. pH-Sensitive Nanomicelles for High-Efficiency siRNA Delivery in Vitro and in Vivo: An Insight into the Design of Polycations with Robust Cytosolic Release. *Nano Lett.* **2016**, *16*, 6916–6923.

- (13) Fukuhara, H.; Yamamoto, S.; Karashima, T.; Inoue, K. Photodynamic Diagnosis and Therapy for Urothelial Carcinoma and Prostate Cancer: New Imaging Technology and Therapy. *Int J Clin Oncol* **2020**, *26*, 18–25.
- (14) Qian, C.; Yu, J.; Chen, Y.; Hu, Q.; Xiao, X.; Sun, W.; Wang, C.; Feng, P.; Shen, Q. D.; Gu, Z. Light-Activated Hypoxia-Responsive Nanocarriers for Enhanced Anticancer Therapy. *Adv. Mater.* **2016**, *28*, 3313–3320.
- (15) Wang, T.; Wang, D.; Yu, H.; Wang, M.; Liu, J.; Feng, B.; Zhou, F.; Yin, Q.; Zhang, Z.; Huang, Y.; et al. Intracellularly Acid-Switchable Multifunctional Micelles for Combinational Photo/Chemotherapy of the Drug-Resistant Tumor. *ACS Nano* **2016**, *10*, 3496–3508.
- (16) Park, H.; Park, W.; Na, K. Doxorubicin Loaded Singlet-oxygen Producing Polymeric Micelle Based on Chlorine e6 Conjugated Pluronic F127 for Overcoming Drug Resistance in Cancer. *Biomaterials* **2014**, *35*, 7963–7969.
- (17) Li, X.; Lovell, J. F.; Yoon, J.; Chen, X. Clinical Development and Potential of Photothermal and Photodynamic Therapies for Cancer. *Nat Rev Clin Oncol* **2020**, *17*, 657–674.
- (18) Zou, Q.; Abbas, M.; Zhao, L.; Li, S.; Shen, G.; Yan, X. Biological Photothermal Nanodots Based on Self-Assembly of Peptide-Porphyrin Conjugates for Antitumor Therapy. *J. Am. Chem. Soc.* **2017**, *139*, 1921–1927.
- (19) Zhu, H.; Cheng, P.; Chen, P.; Pu, K. Recent Progress in the Development of Near-infrared Organic Photothermal and Photodynamic Nanotherapeutics. *Biomater. Sci.* **2018**, *6*, 746–765.
- (20) Tan, X.; Luo, S.; Long, L.; Wang, Y.; Wang, D.; Fang, S.; Ouyang, Q.; Su, Y.; Cheng, T.; Shi, C. Structure-Guided Design and Synthesis of a Mitochondria-Targeting Near-Infrared Fluorophore with Multimodal Therapeutic Activities. *Adv. Mater.* **2017**, *29*, 1704196.
- (21) Larkin, J.; Chiarion-Sileni, V.; Gonzalez, R.; Grob, J. J.; Cowey, C. L.; Lao, C. D.; Schadendorf, D.; Dummer, R.; Smylie, M.; Rutkowski, P.; et al. Combined Nivolumab and Ipilimumab or Monotherapy in Untreated Melanoma. *N Engl J Med* **2015**, *373*, 23–34.
- (22) Wuerstlein, R.; Harbeck, N. Neoadjuvant Therapy for HER2-positive Breast Cancer. *Rev Recent Clin Trials* **2017**, *12*, 81–92.
- (23) Meng, Z.; Chao, Y.; Zhou, X.; Liang, C.; Liu, J.; Zhang, R.; Cheng, L.; Yang, K.; Pan, W.; Zhu, M.; et al. Near-Infrared-Triggered in Situ Gelation System for Repeatedly Enhanced Photothermal Brachytherapy with a Single Dose. *ACS Nano* **2018**, *12*, 9412–9422.
- (24) Min, Y.; Roche, K. C.; Tian, S.; Eblan, M. J.; McKinnon, K. P.; Caster, J. M.; Chai, S.; Herring, L. E.; Zhang, L.; Zhang, T.; et al. Antigen-capturing Nanoparticles Improve the Abscopal Effect and Cancer Immunotherapy. *Nat. Nanotechnol.* **2017**, *12*, 877–882.
- (25) Chen, Q.; Chen, J.; Yang, Z.; Xu, J.; Xu, L.; Liang, C.; Han, X.; Liu, Z. Nanoparticle-Enhanced Radiotherapy to Trigger Robust Cancer Immunotherapy. *Adv. Mater.* **2019**, *31*, No. e1802228.
- (26) Zhang, Y.; Huang, F.; Ren, C.; Yang, L.; Liu, J.; Cheng, Z.; Chu, L.; Liu, J. Targeted Chemo-Photodynamic Combination Platform Based on the DOX Prodrug Nanoparticles for Enhanced Cancer Therapy. *ACS Appl. Mater. Interfaces* **2017**, *9*, 13016–13028.
- (27) Conde, J.; Oliva, N.; Zhang, Y.; Artzi, N. Local Triple-combination Therapy Results In Tumour Regression and Prevents Recurrence in a Colon Cancer Model. *Nat. Mater.* **2016**, *15*, 1128–1138.
- (28) Mura, S.; Nicolas, J.; Couvreur, P. Stimuli-responsive Nanocarriers for Drug Delivery. *Nat. Mater.* **2013**, *12*, 991–1003.
- (29) Rao, L.; Zhao, S. K.; Wen, C.; Tian, R.; Lin, L.; Cai, B.; Sun, Y.; Kang, F.; Yang, Z.; He, L.; et al. Activating Macrophage-Mediated Cancer Immunotherapy by Genetically Edited Nanoparticles. *Adv. Mater.* **2020**, *32*, No. e2004853.
- (30) Zhang, Y.-R.; Luo, J.-Q.; Li, J.-X.; Huang, Q.-Y.; Shi, X.-X.; Huang, Y.-C.; Leong, K. W.; He, W.-L.; Du, J.-Z. Biofunctional Janus Particles Promote Phagocytosis of Tumor Cells by Macrophages. *Chem. Sci.* **2020**, *11*, 5323–5327.
- (31) Yang, C.; Hu, F.; Zhang, X.; Ren, C.; Huang, F.; Liu, J.; Zhang, Y.; Yang, L.; Gao, Y.; Liu, B.; et al. Combating Bacterial Infection by in Situ Self-assembly of AIEgen-peptide Conjugate. *Biomaterials* **2020**, *244*, 119972.
- (32) Tian, L.; Chen, Q.; Yi, X.; Wang, G.; Chen, J.; Ning, P.; Yang, K.; Liu, Z. Radionuclide I-131 Labeled Albumin-Paclitaxel Nanoparticles for Synergistic Combined Chemo-radioisotope Therapy of Cancer. *Theranostics* **2017**, *7*, 614–623.
- (33) Huang, P.; Zhang, Y.; Wang, W.; Zhou, J.; Sun, Y.; Liu, J.; Kong, D.; Liu, J.; Dong, A. Co-delivery of Doxorubicin and (131)I by Thermosensitive Micellar-hydrogel for Enhanced in Situ Synergetic Chemoradiotherapy. *J. Controlled Release* **2015**, *220*, 456–464.
- (34) Babak, M. V.; Zhi, Y.; Czarny, B.; Toh, T. B.; Hooi, L.; Chow, E. K.; Ang, W. H.; Gibson, D.; Pastorin, G. Dual-Targeting Dual-Action Platinum(IV) Platform for Enhanced Anticancer Activity and Reduced Nephrotoxicity. *Angew Chem Int Ed Engl* **2019**, *58*, 8109–8114.
- (35) Wang, Q.; Hou, X.; Gao, J.; Ren, C.; Guo, Q.; Fan, H.; Liu, J.; Zhang, W.; Liu, J. A Coassembled Peptide Hydrogel Boosts the Radiosensitization of Cisplatin. *Chem. Commun.* **2020**, *56*, 13017–13020.
- (36) Zhuang, J.; Gordon, M. R.; Ventura, J.; Li, L.; Thayumanavan, S. Multi-stimuli Responsive Macromolecules and Their Assemblies. *Chem. Soc. Rev.* **2013**, *42*, 7421–7435.
- (37) Musetti, S.; Huang, L. Nanoparticle-Mediated Remodeling of the Tumor Microenvironment to Enhance Immunotherapy. *ACS Nano* **2018**, *12*, 11740–11755.
- (38) Chen, Q.; Liu, G.; Liu, S.; Su, H.; Wang, Y.; Li, J.; Luo, C. Remodeling the Tumor Microenvironment with Emerging Nanotherapeutics. *Trends Pharmacol. Sci.* **2018**, *39*, 59–74.
- (39) Napoli, A.; Valentini, M.; Tirelli, N.; Muller, M.; Hubbell, J. A. Oxidation-responsive Polymeric Vesicles. *Nat. Mater.* **2004**, *3*, 183–189.
- (40) Minotti, G.; Menna, P.; Salvatorelli, E.; Cairo, G.; Gianni, L. Anthracyclines: Molecular Advances and Pharmacologic Developments in Antitumor Activity and Cardiotoxicity. *Pharmacol. Rev.* **2004**, *56*, 185–229.
- (41) Wardman, P. Chemical Radiosensitizers for Use in Radiotherapy. *Clinical Oncology* **2007**, *19*, 397–417.
- (42) Yang, L.; Zhang, C.; Huang, F.; Liu, J.; Zhang, Y.; Yang, C.; Ren, C.; Chu, L.; Liu, B.; Liu, J. Triclosan-based Supramolecular Hydrogels as Nanoantibiotics for Enhanced Antibacterial Activity. *J. Controlled Release* **2020**, *324*, 354–365.
- (43) Ma, N.; Liu, P.; He, N.; Gu, N.; Wu, F. G.; Chen, Z. Action of Gold Nanospikes-Based Nanoradiosensitizers: Cellular Internalization, Radiotherapy, and Autophagy. *ACS Appl. Mater. Interfaces* **2017**, *9*, 31526–31542.
- (44) Rivankar, S. An Overview of Doxorubicin Formulations in Cancer Therapy. *J Cancer Res Ther* **2014**, *10*, 853–858.
- (45) Liu, J.; Wang, H.; Yi, X.; Chao, Y.; Geng, Y.; Xu, L.; Yang, K.; Liu, Z. pH-Sensitive Dissociable Nanoscale Coordination Polymers with Drug Loading for Synergistically Enhanced Chemoradiotherapy. *Adv. Funct. Mater.* **2017**, *27*, 1703832.
- (46) Yi, S.; Allen, S. D.; Liu, Y. G.; Ouyang, B. Z.; Li, X.; Augsornworawat, P.; Thorp, E. B.; Scott, E. A. Tailoring Nanostructure Morphology for Enhanced Targeting of Dendritic Cells in Atherosclerosis. *ACS Nano* **2016**, *10*, 11290–11303.
- (47) Huang, F.; Gao, Y.; Zhang, Y.; Cheng, T.; Ou, H.; Yang, L.; Liu, J.; Shi, L.; Liu, J. Silver-Decorated Polymeric Micelles Combined with Curcumin for Enhanced Antibacterial Activity. *ACS Appl. Mater. Interfaces* **2017**, *9*, 16880–16889.